



## Radiometric comparison of Mars Climate Sounder and Thermal Emission spectrometer measurements

Joshua L. Bandfield<sup>a,\*</sup>, Michael J. Wolff<sup>b</sup>, Michael D. Smith<sup>c</sup>, John T. Schofield<sup>d</sup>, Daniel J. McCleese<sup>d</sup>

<sup>a</sup>Earth and Space Sciences, University of Washington, Seattle, WA 98195-1310, USA

<sup>b</sup>Space Science Institute, Boulder, CO 80301, USA

<sup>c</sup>NASA Goddard Space Flight Center, Greenbelt, MD 20770, USA

<sup>d</sup>Jet Propulsion Laboratory, California Institute of Technology, CA 91109, USA

### ARTICLE INFO

#### Article history:

Received 18 December 2012

Revised 28 February 2013

Accepted 1 March 2013

Available online 25 March 2013

#### Keywords:

Mars, Climate

Infrared observations

Mars, Atmosphere

### ABSTRACT

Mars Climate Sounder (MCS) nadir oriented thermal infrared and solar channel measurements are compared with Thermal Emission Spectrometer (TES) measurements across multiple Mars years. Thermal infrared measurements were compared by convolving the TES data using the MCS spectral band passes. The MCS solar channel measurements were calibrated using Compact Reconnaissance Imaging Spectrometer for Mars observations to provide the proper gain factor ( $3.09 \times 10^{-3} \text{ W sr}^{-1} \text{ m}^{-2} \mu\text{m}^{-1}$ ). The comparisons of the datasets show that day and night surface and atmospheric temperatures are within 3 K over the course of 5 martian years, after accounting for the local time differences. Any potential interannual variations in global average temperature are masked by calibration and modeling uncertainties. Previous work attributed apparent interannual global surface and atmospheric temperature variations to major dust storm activity; however, this variation has since been attributed to a calibration error in the TES dataset that has been corrected. MCS derived Lambert albedos are slightly higher than TES measurements acquired over the same season and locations. Most of this difference can be attributed to the spectral response functions of MCS and TES. Consistent with previous work, global albedo is highly variable ( $\sim 6\%$ ) and this variability must be taken into account when determining long term global trends. Vertical aerosol distributions were also derived from the calibrated MCS visible channel limb measurements, demonstrating the utility of the MCS visible channel data for monitoring of aerosols.

© 2013 Elsevier Inc. All rights reserved.

### 1. Introduction

In order to understand the cycles, trends, and variability of the current martian climate, it is necessary to build a long-term record of global surface and atmospheric properties. This includes global monitoring of visible wavelength albedo, surface and atmospheric temperatures, and atmospheric aerosol and water vapor properties. A multi-annual, systematic series of well-calibrated observations is also crucial to discerning the links between various systems and how their correlations contribute to the observed regional and global weather, such as the planet encircling dust events that continue to defy predictability.

Infrared spectral observations (within the wavelength range of  $\sim 5\text{--}50 \mu\text{m}$ ) have been collected by orbiting spacecraft from the Mariner 9 Infrared Interferometer Spectrometer (IRIS) and the Viking Infrared Thermal Mapper (IRTM) instruments during the 1970s to the current Mars Reconnaissance Orbiter (MRO), Mars Climate

Sounder (MCS). In addition, limited atmospheric temperature profiles have been collected via microwave, and entry decent and landing (EDL) measurements (e.g. Hinson et al., 1999; Withers and Smith, 2006). Despite the variety of long term measurements spanning several decades, systematic global observations were not collected until the start of the primary mapping phase of the Mars Global Surveyor (MGS), Thermal Emission Spectrometer (TES) investigation. Even in the case of the Viking IRTM measurements that were collected from 1976 to 1980, there are significant gaps in spatial/seasonal coverage for a given local time (e.g., Martin, 1981; Wilson and Richardson, 2000).

Despite these limitations, several studies have assembled inter-annual comparisons in order to characterize various aspects of the current martian climate (e.g., Jakosky and Farmer, 1982; Martin and Richardson, 1993; Cantor et al., 2002; Smith, 2004). For example, Martin and Richardson (1993) and Smith (2004) focused on multiannual observations with the IRTM and TES datasets, respectively. Other studies compared multiple datasets and incorporated general circulation models (GCMs) in order to cover greater time periods or to better understand the accuracy of the measurements (e.g., Richardson, 1998; Clancy et al., 2000; Wilson and Richardson,

\* Corresponding author.

E-mail address: [joshband@u.washington.edu](mailto:joshband@u.washington.edu) (J.L. Bandfield).

2000; Liu et al., 2003; Fenton et al., 2007). These studies have shown both repeatable characteristics of the current martian climate (such as the aphelion water ice cloud belt) as well as highly variable characteristics (such as the timing and extent of major dust events). However, questions have also been raised regarding the calibration accuracy of the measurements themselves (Clancy et al., 2000; Wilson and Richardson, 2000) that can make the interpretation of interannual variations suspect even within individual datasets. As a result, it is still not clear what the magnitude of true interannual variation is on Mars. For example, the extent and magnitude of regional and global dust events can clearly have large and variable effects on global temperatures and albedos, but the longer term effects on global temperatures remain unclear.

In this work, we limit our investigation to the calibration and comparison of surface and atmospheric radiance derived from the TES and MCS datasets. We describe the calibration of the MCS visible bolometric channels, correction of systematic TES calibration errors, and compare the measured nadir oriented radiance from all MCS channels to TES measurements. There are two questions that we attempt to address:

- (1) What level of precision and accuracy is achievable with the recent measurements within and between the spacecraft datasets?
- (2) Are there detectable interannual variations in albedo and global temperatures on Mars?

Answering these questions requires a great deal of focus on details of calibration and observation conditions.

## 2. Instrument and dataset characteristics and calibration

### 2.1. MCS

#### 2.1.1. Instrument and operations description

The Mars Climate Sounder (MCS) on the Mars Reconnaissance Orbiter (MRO) began acquiring near-continuous measurements of Mars in 2006. The MCS investigation goals are to characterize the thermal structure of the atmosphere and the vertical distribution of its aerosols and water vapor. In addition, surface measurements have been acquired to characterize the polar radiative balance through measurements of the angular dependence of emitted and reflected radiance at the top of the martian atmosphere. The surface and atmospheric measurements together can constrain and characterize the current climate of Mars.

The MCS instrument has a total of 9 linear arrays, each consisting of 21 thermopile detectors at the focal plane of two symmetrical off axis telescopes. Each detector has a 3.3 by 6.2 mrad field of view (FOV) with a 2.048 s integration time that allows for ~5 km vertical sampling at the limb tangent point from the ~280 km MRO mapping orbit. Nadir observations have a 1.5 by ~8 km sampling with the elongation due to spacecraft motion. Glass, multi-layer interference, and wire mesh (copper grids and squares deposited on polypropylene substrates) spectral filters are arranged in front of each of the detector arrays (McCleese et al., 2007). There are six spectral channels in the focal plane of the A telescope that consists of mid-infrared channels and the visible/near-infrared bolometric channel. The B telescope consists of the three longer wavelength infrared channels (Fig. 1). Spectral band pass characteristics vary slightly between detectors within the B channels because of the characteristics of the wire mesh filters.

The planned typical mapping observation strategy of MCS consists of forward limb staring measurements with periodic nadir and space observations in a 34 s cycle. “Buckshot mode” observations, which consist of using the 2-axis pointing capability of

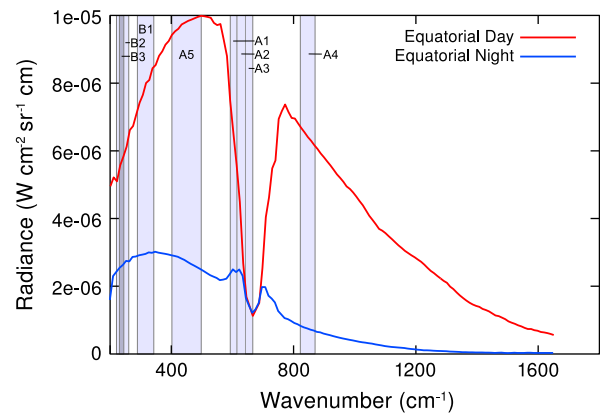


**Fig. 1.** Typical TES radiance spectra (nadir-oriented within 5° of the equator from TES OCKs 1907–1918;  $L_s$  116, MY 24) with the full width at half maximum transmission MCS band-passes shown in gray. MCS channels B2 and B3 have overlapping spectral coverage with channel B3 covering a narrower spectral range than channel B2. The spectral coverage of MCS channels A1–3 are within the  $\text{CO}_2$  fundamental absorption and are relatively insensitive to radiance from the martian surface.

MCS to cover a widespread area, occur periodically near the poles. Details of the MCS instrument characteristics and observing strategy are described in McCleese et al. (2007).

Position errors in the MCS elevation actuator increased in frequency after the start of mapping operations and regular nadir observations were discontinued. As a result, the data used for this study are limited to the nadir and limb observations acquired during the period from September 2006 to January 2007. Despite the lack of nadir-oriented observations, limb-staring observations have continued and off-nadir surface measurements have been systematically acquired. Although the comparisons presented here do not include off-nadir data, the relative accuracy determined from our work is applicable to the off-nadir dataset.

#### 2.1.2. Calibration of MCS visible channel measurements

Calibration of the MCS visible wavelength channel (A6) was planned to use views of space and the MCS solar target to provide a full-aperture 2-point calibration assuming a linear instrument response. The solar target is a textured aluminum plate that was intended to provide nearly Lambertian scattering of solar radiance.

In practice, energy reflected of the aluminum plate varies significantly with emergence angle and a more complex calibration scheme is required. Laboratory measurements of the solar target reflectance over a range of illumination angles were acquired at an incorrect emergence angle. In addition, stray solar light reflected from the MCS instrument can influence measured radiance from the target. These properties greatly complicate the use of the solar target for calibration purposes because it requires characterization of the reflective behavior of the target using the uncalibrated visible channel measurements themselves. As a result, space views can be used to determine offsets and the target can be used to correct for gain differences between detectors, but absolute gain cannot be established.

Special observations were acquired to determine and remove the relative gain differences between detectors. The gains of each of the channel A6 detectors are scaled so that they are all the same as channel A6, detector 11 (A6D11), using a set of observations of the solar target at slightly different elevation angles so that the spatial coverage of A6D01, A6D11, and A6D21 were superimposed. This accounts for non-uniform target illumination and reflectivity across the array. These steps reduce the data to a set of unitless “counts” (total number for the 2 s observation, rather than a count

rate) where the zero level is set and gain levels for all detectors have been normalized to that of A6D11.

It is also necessary to find the proper multiplicative gain factor to convert the counts to a known quantity of radiance. Fortunately, the Compact Reconnaissance Imaging Spectrometer for Mars (CRISM; Murchie et al., 2007) is also present on MRO and acquires data covering a similar wavelength range as that of the MCS visible channel (Fig. 2). More specifically, it is possible to combine CRISM multispectral (MSP) mapping mode observations (~100–200 m/pixel, 72 wavelengths; Murchie et al., 2007) with (near-)coincident MCS observations using knowledge of the MCS visible channel band pass. Given that CRISM MSP observations are typically obtained in a nadir orientation, we constructed our observational sample from the period associated with the largest number of MCS nadir measurements; September 24, 2006 to January 18, 2007.

To minimize issues associated with surface and atmospheric inhomogeneity at the mesoscale, we summed CRISM data in the cross-track direction to approximately 20 km per spectral “pixel”. Though this is coarser than the MCS spatial resolution, this “framelet” size has been used in several projects to provide a useful balance between resolution and data volume. For the selected time period, more than 1.5 million CRISM MSP framelets are present. Matching MCS observations are identified for each framelet by specifying minimum differences in the spacecraft clock time and the framelet/detector centroid viewing geometry. The former criterion and our choice of 30 s quickly reduces the possible matching observations to an “in the ballpark” subsample. For viewing geometry, we combine minimum differences in latitude and longitude ( $\Delta\text{lat}$  and  $\Delta\text{lon}$ ) with constraints on surface emergence and solar incidence angles ( $\Delta\text{ema}$  and  $\text{inamax}$ ). For a framelet to be further considered, we required that it has at least 5 MCS detectors from a single acquisition time that meet the viewing geometry constraints. Finally, matching CRISM radiance measurements are convolved using the MCS channel A6 response function. The resulting multiplicative gain factor necessary to convert MCS visible channel counts to radiance was calculated by simply dividing the mean CRISM derived radiance values with their associated MCS channel A6 counts.

To summarize, the center point geometry information for each  $\sim 20 \times 0.2$  km CRISM “pixel” is compared to the center location of

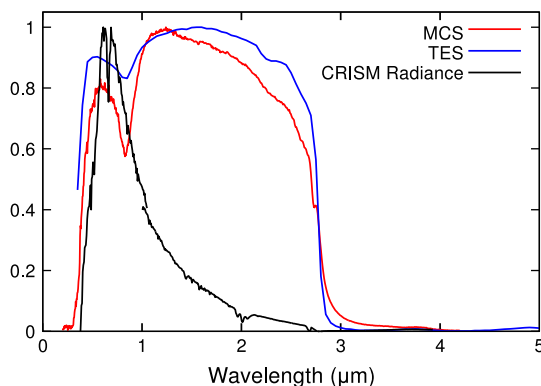


**Fig. 2.** MCS and TES visible/near-infrared channel spectral response functions normalized to unity at maximum throughput and typical martian radiance (also normalized to unity) as measured by CRISM (FRT0000B141\_07, centered near 24°E, 19°S). The greater throughput of the TES visible bolometer response function at visible wavelengths relative to MCS places a greater emphasis on visible wavelength reflectivity of the martian surface. This results in lower derived Lambert albedos in TES data (~3%) because the martian surface typically has a lower reflectivity at visible wavelengths than at near-infrared wavelengths. The discontinuity in the CRISM radiance near 1  $\mu\text{m}$  is caused by the use of separate detector arrays within each wavelength region.

each 1.5 by 8 km MCS measurement. Our viewing geometry constraints include  $\Delta\text{lat} = 0.2^\circ$  (~12 km),  $\Delta\text{lon} = 0.3^\circ$  (~12–18 km),  $\Delta\text{ema} = 2^\circ$ , and  $\text{inamax} < 60^\circ$ . The requirement that at least 5 MCS detectors from a single acquisition time fit the constraints forces significant cross track overlap between the two measurements.

These constraints produce a sample of 22,141 framelets and a radiometric coefficient of  $3.08 (\pm 0.27 \text{ standard deviation}) \times 10^{-3} \text{ W sr}^{-1} \text{ m}^{-2} \mu\text{m}^{-1}$  per MCS count. Examining the scatter about the mean value indicates that about 50% of the standard deviation is carried by a small number of outliers. Employing a three-sigma rejection criteria eliminates only 600 points, but significantly improves the precision:  $3.09 (\pm 0.15) \times 10^{-3} \text{ W sr}^{-1} \text{ m}^{-2} \mu\text{m}^{-1}$  per MCS count with essentially no change in the mean value. Tighter constraints on the viewing geometry do not appreciably change the results.

An additional factor to be examined is that of the dispersion in the individual MCS detector values associated with each CRISM framelet. That is to say, the FOV of the detectors that make up the average from each radiometric coefficient calculation may be seeing inhomogeneity that is averaged in the lower spatial resolution CRISM product. The standard deviation of the MCS measurements associated with each CRISM framelet is also calculated. For example, adopting either 3% or 5% limits for the relative MCS standard deviation (reasonable values given the observed radiometric stability of the MCS visible channel) would indicate that any values greater than this are due to scene rather than instrumental variability. These two standard deviation cut-offs (each leave more than 20,000 points in the sample), do not dramatically change the coefficients:  $3.09 (\pm 0.14) \times 10^{-3} \text{ W sr}^{-1} \text{ m}^{-2} \mu\text{m}^{-1}$  per MCS count and  $3.10 (\pm 0.13) \times 10^{-3} \text{ W sr}^{-1} \text{ m}^{-2} \mu\text{m}^{-1}$  per MCS count respectively. Other restrictions, such as using only spatially uniform areas or limiting solar incidence angles may be employed to further reduce the standard deviation. However, our constraint tuning and other filtering methods affect the radiometric coefficient at significantly less than the 1% level with respect to our initial calculation, which is significantly lower than other formal uncertainties.

The absolute accuracy of our coefficient is limited by that of the CRISM observations themselves. Murchie et al. (2007) report absolute and relative radiometry limits of 10% and 5%, respectively. However, these may be overly conservative. Bell et al. (2009) perform a cross-comparison exercise for the Mars Color Imager (MARCI) camera system (also aboard MRO) similar to ours described above. An important difference in the MARCI case is that the visible imaging was calibrated independently using ground-based observations. Consequently, a comparison of the MARCI pre-launch and CRISM-based radiometric coefficients provides an estimate of the CRISM accuracy. Bell et al. (2009) find an agreement of better than 3–5% between the two methods. This suggests that assigning an accuracy of 5% to the MCS radiometry is not unreasonable.

## 2.2. TES

### 2.2.1. Instrument and operations description

The TES instrument is a Fourier transform Michelson interferometer (covering ~6–50  $\mu\text{m}$  wavelengths) with co-aligned thermal (5–100  $\mu\text{m}$ ) and visible (0.3–3  $\mu\text{m}$ ) bolometers. The detectors are arranged in a 3 by 2 array, each with an 8 mrad instantaneous FOV with a 1.8 s integration time (Christensen et al., 1992). This configuration results in a 3 by ~8 km footprint from the ~380 km MGS mapping orbit with the elongation due to smear from the lack of image motion compensation. A pointing mirror allows for along track targeting capability as well as viewing of the limb, space, and an internal reference surface.

Typical mapping configuration observations consisted of continuous nadir observations with limb scanning observations interspersed every  $\sim 3$  min ( $\sim 10^\circ$  lat). Limb observations were offset between orbits to avoid gores in nadir coverage. Special observations, such as emission phase function measurements, were relatively rare and occurred during a limited period about once every orbit. A primary goal of the observing strategy was to build a continuous, systematic, and global set of measurements. Details of instrument calibration and observations are described in Christensen et al. (2001). Three martian years of nearly continuous spectrometer observations were collected from the MGS mapping orbit from February 1999 to September 2004, when degradation of the neon lamp used for tracking interferometer motion prevented continued use of the spectrometer. Gaps in data collection up to several weeks in duration occurred during solar conjunction, spacecraft safe mode, and other similar types of events.

### 2.2.2. TES calibration space observation correction

Starting on OCK (Orbit Counter Keeper; the orbit number starting at Mars orbit insertion rather than the start of the MGS mapping mission) 12,581 ( $L_s$  215, MY 25), the normal MGS mapping orientation was rotated  $16^\circ$  as a fuel saving measure. As a result, TES could no longer use the  $-90^\circ$  pointing angle for the space view used for calibration because a portion of Mars could find its way into the FOV. With this spacecraft orientation change, the space view was switched to a  $+74^\circ$  pointing angle that would ensure that Mars would not enter into the TES FOV for the space calibration observations. Unfortunately, the TES pointing mirror is only designed to clear the shroud from pointing angles of  $-90^\circ$  to  $+70^\circ$ . Observations that stepped the mirror at  $1^\circ$  intervals confirm that all six detectors from the spectrometer do not experience vignetting to a pointing angle of no more than  $+72^\circ$ . At the pointing angle of  $+74^\circ$  used for TES OCKS 12,581–26,794 ( $L_s$  215, MY 25 to  $L_s$  103, MY 27), TES detectors 3 and 6 detect an additional  $4.5 \times 10^{-7}$  and  $2 \times 10^{-7} \text{ W cm}^{-2} \text{ sr}^{-1} \text{ cm}$  respectively between 400 and  $800 \text{ cm}^{-1}$  (Fig. 3). This effect is less for detectors 2 and 5 ( $1 \times 10^{-7} \text{ W cm}^{-2} \text{ sr}^{-1} \text{ cm}$ ) and is not present in TES detectors 1 and 4. There does not appear to be any effect on the TES visible and thermal bolometers. The result is an apparent negative radiance for cold temperature observations, such as space, polar caps, and the martian atmosphere.

The magnitude of this error on the calibrated radiance data is dependent on the wavenumber and magnitude of radiance of the target. The largest errors are near  $600 \text{ cm}^{-1}$  and for cold targets.

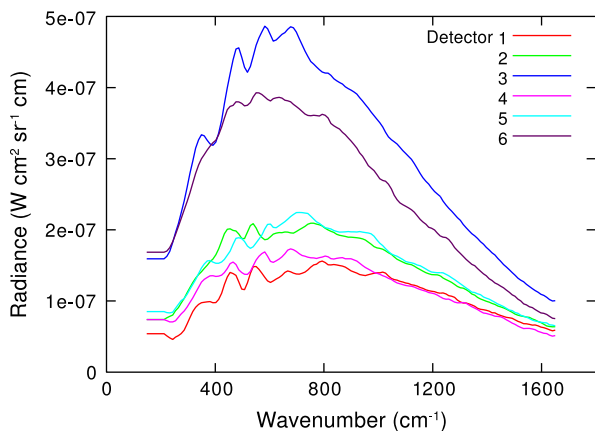


**Fig. 3.** Average TES radiance values for each detector due to the calibration observation errors at TES mirror pointing angles of  $+74^\circ$ . This error results from a portion of the instrument shroud in the field of view. These radiance values are used to correct the TES data, making them consistent with the  $-90^\circ$  pointing angle calibration observations.

Polar/nighttime surface temperature determination and atmospheric temperature retrievals are significantly affected and warm surface temperature, atmospheric opacity retrievals, and spectroscopic investigations are not affected in a significant manner. There are several reasons for this, including the diminishing relative and absolute magnitude of the error with increasing signal. Temperature errors at  $667 \text{ cm}^{-1}$  (at the center of the  $\text{CO}_2$  fundamental absorption) for an average of all six detectors are  $-3 \text{ K}$ ,  $-4 \text{ K}$ , and  $-8 \text{ K}$  for 200, 180, and  $150 \text{ K}$  temperatures respectively. At  $250\text{--}450 \text{ cm}^{-1}$  these errors are somewhat lower;  $-2$  to  $-4 \text{ K}$ .

The radiance inaccuracies listed above can be corrected in a relatively simple manner. Rather than assuming that observations of space are a zero radiance target, the TES calibration software has been modified to change this assumption to a constant radiance as a function of wavenumber and detector for space calibration observations acquired at a mirror pointing angle of  $+74^\circ$ . This constant radiance was obtained from large averages of  $-90^\circ$  pointing angle space calibration observations acquired after OCK 16,887 ( $L_s$  48, MY 26) but before an additional time variable radiance error appeared in the data near OCK 19,000 ( $L_s$  126, MY 26; not discussed here). These  $-90^\circ$  pointing angle observations were acquired on the nighttime side of the planet when the MGS spacecraft was reoriented from the  $16^\circ$  fuel saving orientation to nadir pointing during reaction wheel desaturation events. The constant radiance values were obtained using data that has been reprocessed using only  $+74^\circ$  space observations to allow the  $-90^\circ$  space observations to be calibrated relative to the  $+74^\circ$  observations. The large averages reduce the sample to sample random noise of the instrument to insignificant levels.

The result of this correction has been to modify the calibration scheme to produce data for the entire mission that are similar to the traditional  $-90^\circ$  space calibration observations acquired until OCK 12,581. This ensures that the TES calibrated radiance data is accurately calibrated throughout the mission and consistent within each orbit with the initial nadir spacecraft observation configuration. All TES radiance data used for this study were processed using calibration version 2e and are identical to the data available at the Planetary Data System at the time of publication. No additional corrections were applied to the TES data.

A slight misalignment of the TES secondary mirror results in an additional radiance error (Christensen et al., 2001) that remains uncorrected in the data used for this study. This error, colloquially known as “COBE”, is inversely proportional to the ratio of scene radiance relative to that of the instrument (approximated by a  $300 \text{ K}$  blackbody). It is also dependent on detector, wavenumber, and mirror pointing angle. For the data used for this study, errors are less than  $+0.25\text{--}0.5 \text{ K}$  at wavelengths corresponding to MCS channels 1–3 (within the  $15 \mu\text{m}$   $\text{CO}_2$  fundamental absorption). Errors are estimated to be  $+0.25\text{--}1 \text{ K}$  for day and night observations at wavelengths corresponding to MCS channels B1–3 and A4 ( $>20 \mu\text{m}$ ). Larger errors are present at wavelengths corresponding to MCS channel A5 ( $\sim 11\text{--}12 \mu\text{m}$ ), ranging from  $+0.5\text{--}0.75 \text{ K}$  at  $240 \text{ K}$  to  $+1.5\text{--}2 \text{ K}$  at  $180 \text{ K}$ .

## 3. Methods

### 3.1. Comparison of thermal infrared measurements

#### 3.1.1. Convolution of TES data with MCS band passes

Comparison of the measured radiance is the most direct means of determining the extent of interannual climate variability. Subsequent processing to derive surface kinetic temperatures, atmospheric temperature profiles, or other properties will typically be performed via slightly different methods depending on the properties of the dataset. These methods are likely to interfere with the

comparison between datasets. The MCS and TES datasets used here were limited to a  $L_s$  range of 105–145 because of the limited period of MCS nadir observations and because the seasonal range is generally free of highly variable dust events. The isolation of the data from limited duration weather events makes it simpler to identify any longer-term variability or systematic differences between the two datasets.

We convolved the TES radiance data using the MCS band pass filter functions (available at the Planetary Data System) to produce the most direct comparison of TES and MCS data possible. Slight variations exist in the TES wavenumber scale for each of the six detectors due to self-apodization. To match the filter functions to the TES spectral sampling, we performed a spline fitting of each MCS filter function to the center wavenumber sampling for TES detector 2. The wavenumber scale of TES detector 2 reasonably approximates the scale for all six detectors and the difference between the wavenumber samples of the 6 detectors is  $<2 \text{ cm}^{-1}$  at  $1000 \text{ cm}^{-1}$  and progressively diminishes to  $<0.5 \text{ cm}^{-1}$  at  $200 \text{ cm}^{-1}$ . In addition, the 3 average MCS B channel band passes (Fig. 1) were used for convolution rather than individually comparing the 63 separate detectors within the three channels.

These approximations have little effect when comparing relatively broad wavelength spectral observations. However, complications can occur when determining properties from narrow spectral absorptions. For example narrow water vapor lines require wavenumber scale characteristics to be accurately defined beyond the levels used here (Smith, 2002). In order to accurately compare water vapor measurements between MCS and TES, it is necessary to account for the individual wavenumber scales of all TES and MCS detectors and is beyond the scope of this work.

After convolution, all TES and MCS measurements were averaged into separate ascending and descending (day and night) orbit bins of  $5^\circ$  latitude,  $10^\circ$  longitude, and  $5^\circ$  of  $L_s$ . All data were restricted to emission angles of  $<30^\circ$  and the TES data were also restricted based on several quality flags. Comparisons were made between Mars Years (MY) 24–26 (TES; MY 26 was limited to  $L_s$  110–130) and 28 (MCS). Data from early in the MGS mission (MY 24–25) are more reliable because observations were more consistent, free of known systematic errors, and the calibration was more stable. For the comparisons discussed in this work, all longitudes were averaged.

### 3.1.2. Accounting for local time differences

The largest potential discrepancy between the TES and MCS measurements is due to the 1 h difference in the fixed local time orbits of MGS ( $\sim 2$  AM/PM) and MRO ( $\sim 3$  AM/PM). The effect of this difference is greatest for afternoon surface temperatures, but is also potentially significant for atmospheric temperatures and nighttime surface temperatures.

A relatively simple method for accounting for the difference in the local time of the observations is to use a thermal model to predict the expected surface temperature differences. We use the krc thermal model (Kieffer, 2013), which has been used for a variety of martian thermophysical applications (e.g., Titus et al., 2003; Ferguson et al., 2006; Bandfield and Edwards, 2008; Bandfield and Feldman, 2008). In this application, longitudinally averaged surface temperatures were modeled using local elevation, albedo, and thermal inertia input along with assumed constant visible wavelength dust opacity of 0.30.

There are many uncertainties associated with predicting martian surface temperatures, especially for daytime observations where uncertainties in atmospheric properties have the greatest effect on the energy balance (e.g., Bandfield and Edwards, 2008; Bandfield and Feldman, 2008). The uncertainties associated with modeling surface temperatures (especially when based on thermophysical properties derived from the models and measurements

themselves) are several degrees Kelvin and may be as large as 5–10 K for daytime observations. These uncertainties would preclude the accurate determination of any interannual variations, which are likely to be significantly smaller.

The modeled changes in temperature with time of day are more accurate than the absolute modeled temperatures (Bandfield and Edwards, 2008), allowing for precise comparisons between the 2–3 AM/PM local times of the MCS and TES measurements. Table 1 provides examples of the effects of uncertainties in surface and atmospheric properties on the modeled temperature changes. The examples explore the effects of errors in surface thermal inertia of  $50 \text{ J m}^{-2} \text{ K}^{-1} \text{ s}^{-1/2}$  and visible wavelength opacity of 0.15. Both of these ranges are significant but not unreasonable uncertainties in the various properties. The resulting differences in the predicted 2–3 AM/PM changes in surface temperatures vary by three orders of magnitude depending on the local time and latitude, but all are less than 1 K. Uncertainties in surface albedo affect modeled daytime surface temperatures in a manner similar to uncertainties in dust opacity. Surface temperature changes are generally more stable when energy input conditions are not highly variable, such as nighttime observations at the equator (Table 1).

Atmospheric temperatures and water ice aerosol abundances may also have significant differences between the 2–3 AM/PM observations. Accounting for these changes may be considerably more difficult. For example, the diurnal variation of martian water ice aerosols is still being documented (Curran et al., 1973; Petrova et al., 1996; Zasova et al., 2001; Tamppari et al., 2003; Glenar et al., 2003; Madeleine et al., 2012) and it is possible that changes may occur that would significantly alter measured radiance at wavelengths where water ice absorptions occur (e.g., 11 and  $40 \mu\text{m}$ ; Wilson et al., 2007). Even without any change in surface temperature, significant differences in brightness temperature could be present. This effect can be detected by observing the behavior of any differences in the comparisons within and outside of the absorption wavelength regions. Regardless, there is potential for the differences in the predicted 2–3 AM/PM temperatures to have errors larger than indicated by the estimated uncertainties listed in Table 1.

Atmospheric temperatures also change by up to  $\pm 1$  K at altitudes up to  $\sim 35$  km. This difference diminishes with increasing distance from the equator for the period of comparisons shown here (e.g., Wilson and Richardson, 2000). This effect is negligible for MCS channels that fall outside the  $15 \mu\text{m}$   $\text{CO}_2$  absorption, but will directly affect the brightness temperatures in MCS channels A1–3.

### 3.2. Comparison of MCS and TES visible channel measurements

The wavelength dependent response of the MCS and TES visible channels are similar, but not coincident (Fig. 2), and the variable local times of the MGS and MRO orbits preclude direct comparison of the TES and MCS measured radiance. A comparison may be made by converting the measured radiance to Lambert albedo using the following relationship:

$$A = \pi \cdot R_{\text{meas}} / [(R_{\text{solar}} / d^2) \cdot \cos Z], \quad (1)$$

**Table 1**

Effects of uncertainties in surface thermal inertia (TI) and atmospheric opacity ( $\tau_{\text{vis}}$ ) on the modeled surface temperature change between 2 and 3 AM/PM.

Starting conditions: $\tau_{\text{vis}} = 0.15$ , TI = 200	$\Delta T$ $0^\circ\text{N}$	$\Delta T$ $60^\circ\text{N}$
Change $\tau_{\text{vis}}$ to 0.30 (LT 0200–0300)	0.06 K	0.01 K
TI to 250 (LT 0200–0300)	0.001	0.27
$\tau_{\text{vis}}$ to 0.30 (LT 1400–1500)	0.19	0.07
TI to 250 (LT 1400–1500)	0.94	0.48

where  $A$  is the Lambert albedo,  $R_{meas}$  is the measured MCS or TES solar band radiance,  $R_{solar}$  is the solar irradiance at 1 AU convolved using the MCS and TES filter functions (489.845 and 519.525  $W m^{-2} \mu m^{-1}$ , respectively),  $d$  is the solar distance in AU, and  $z$  is the solar zenith angle.

Although no surface is perfectly Lambertian, the effect of this assumption is comparable for both measurements because of the similarity in observing phase angles (within  $\sim 15^\circ$ ) between the MGS and MRO orbits. Because the response function of the MCS and TES visible channels are slightly different and martian reflectance is wavelength dependent, there will also be differences in derived albedo even under identical viewing conditions. The spectral response of the TES visible bolometer has a greater relative weight at shorter wavelengths compared to the MCS visible channel response (Fig. 2). This difference results in shorter wavelengths hav-

ing a greater influence on the TES measurements. Because Mars typically has a relatively low reflectivity at wavelengths less than  $\sim 0.9 \mu m$ , the TES derived albedos will be slightly lower than MCS derived albedos for a given surface. Using CRISM scene 0000B141\_07 as an example of known wavelength dependent radiance and convolving this radiance with the TES and MCS visible channel spectral responses, derived Lambert albedo values are 0.148 and 0.144 for MCS and TES respectively. The CRISM image is centered near 341E, 24N with and is typical of moderate albedo regions on Mars. This  $\sim 3\%$  (proportional) difference is expected to be present for most martian surfaces.

The derived Lambert albedos were binned at 1 pixel per degree and  $15^\circ$  of  $L_s$  from the same seasonal range as with the TIR comparisons. Data were restricted to solar incidences of  $< 88^\circ$  and emission angles of  $< 30^\circ$ . Comparisons were made between MY 24–27 (TES)

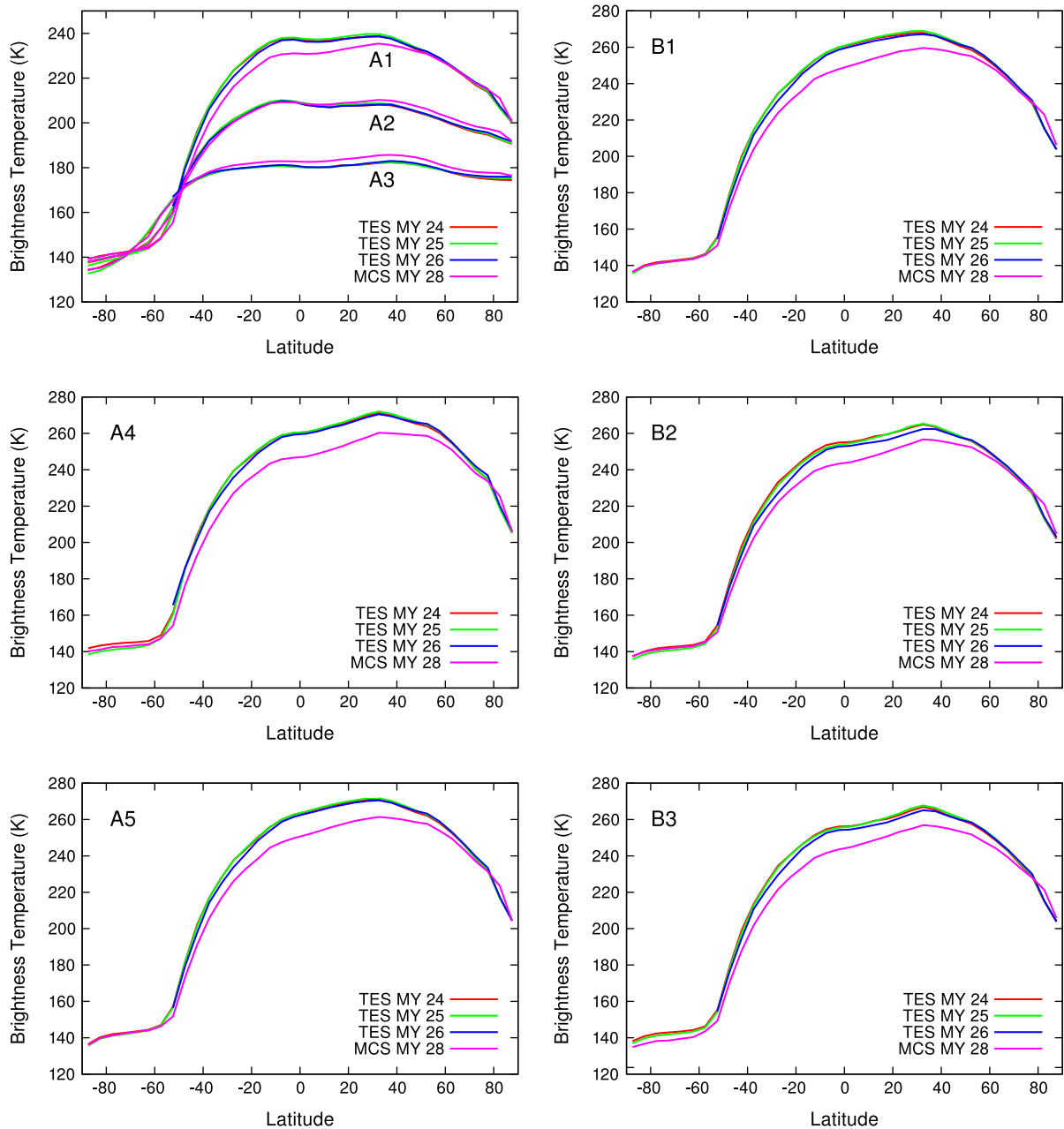


**Fig. 4.** Longitudinally averaged (latitude zonal mean) daytime brightness temperatures for MCS data and TES data convolved to the MCS band-passes. Data cover  $L_s$  105–145 (MY26 is limited to  $L_s$  110–130). Significant differences between TES and MCS data in channels A4–5 and B1–3 are due to the later local time of MCS measurements. Water-ice clouds cause the slightly lower brightness temperatures between  $5^\circ S$  and  $25^\circ N$  in channels A4 and B2–3.

and 28 (MCS) because the visible bolometer measurements appear to have remained stable throughout the MGS mission.

### 3.3. Retrieval of limb aerosol abundances using MCS visible channel measurements

As a proof of concept for studies of detached aerosol layers, we retrieve the extinction profiles (optical depth per kilometer) from a set of solar band observations where the apparent height of the layer evolves with spacecraft motion. Using a Gauss-Seidel Limb Scattering radiative transfer algorithm for a spherical shell geometry provided by D. Flittner (GSSRTM version 4.5, e.g., Herman et al., 1994, 1995; Loughman et al., 2004), we calculate the observed radiance using the geometry reconstructed for each observed profile, smoothed to an effective resolution of 5 km. We assume a single aerosol component whose scattering properties are represented by a dust model with an average particle radius of 1.5  $\mu\text{m}$  (Wolff et al., 2009). Finally, the surface albedo is taken from

an atmospherically-corrected TES solar band albedo map (Wolff et al., 2006).

We obtain the extinction factors on a grid with 7-km spacing using a non-linear fitting routine (MPFIT, an IDL version of the MINPACK-1 routine; Moré, 1978; Markwardt, 2009) that makes direct calls to the radiative transfer model described above. The lowest fit point is 7 km, with values below this level being linearly-extrapolated with pressure. Given the artifice of assuming a single aerosol composition and a fixed particle size, the resulting profiles should be regarded as qualitative in nature.

## 4. Results

### 4.1. Thermal infrared measurements

Longitudinally averaged brightness temperatures are shown in Figs. 4 and 5 and Table 2. Several bands have little variation between MY 24–28 MCS/TES measurements. For example, TES/MCS

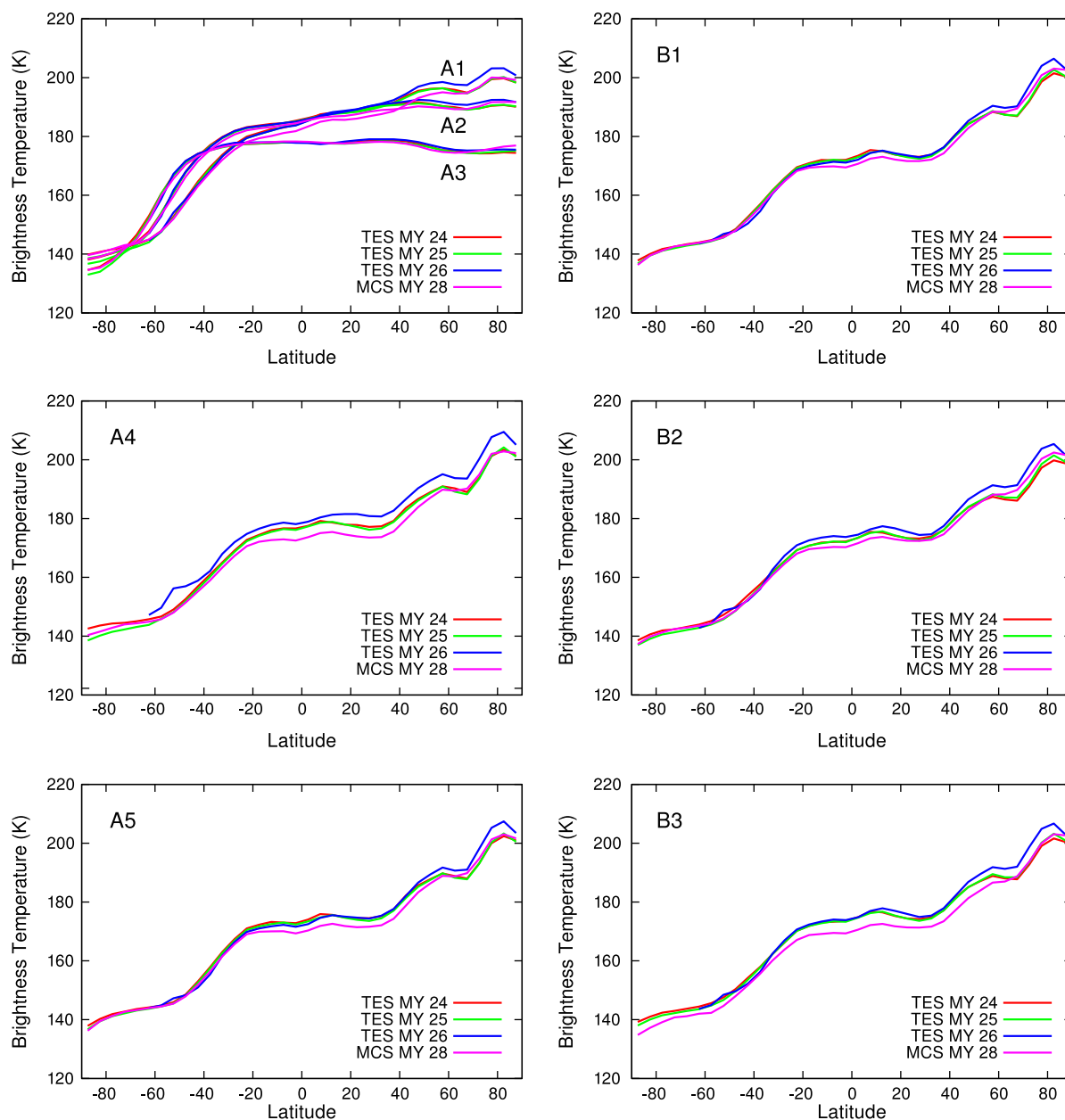


**Fig. 5.** Longitudinally averaged nighttime brightness temperatures for MCS data and TES data convolved to the MCS band-passes. Data cover  $L_s$  105–145 (MY26 is limited to  $L_s$  110–130). Significant differences between TES and MCS data in channels A4–5 and B1–3 are due to the later local time of MCS measurements.

**Table 2**

Global average brightness temperatures equatorward of 60° latitude for the period of  $L_s$  105–145. Significant differences between MCS and TES measurements are largely due to local time observational differences. TES measurements from Mars Year 26 (italicized) have increased calibration uncertainties and cover  $L_s$  110–130 resulting in relatively large temperature differences, especially at shorter wavelengths (channel A4) and daytime temperatures (daytime channels A4–5 and B1–3). The MCS (LT Adjusted) column accounts for modeled local time differences in surface temperature between the MCS and TES observations.

MCS channel (daytime)	TES MY 24	TES MY 25	TES MY 26	MCS MY 28	MCS (LT adjusted)
A1	225.1 K	225.5	223.2	220.1	
A2	201.2	201.6	200.2	201.4	
A3	178.9	178.9	178.9	181.1	
A4	246.9	247.2	244.9	236.0	245.0
A5	247.0	247.4	244.4	237.1	246.1
B1	244.2	244.6	241.2	235.2	244.2
B2	240.8	240.1	236.2	232.0	241.0
B3	242.1	242.1	238.2	231.8	240.8
MCS channel (nighttime)					
A1	181.9	181.6	182.0	179.5	
A2	183.7	183.4	183.7	182.2	
A3	176.5	176.3	176.7	176.0	
A4	173.6	173.1	176.4	170.4	171.3
A5	170.9	170.5	170.4	168.2	169.1
B1	169.9	169.6	169.5	168.1	169.0
B2	170.0	169.8	171.4	168.5	169.4
B3	171.0	170.9	171.6	167.4	168.3

channel A3 (near the center of the CO<sub>2</sub> fundamental absorption) nighttime measurements vary from 176.0 to 176.7 K. By contrast, TES/MCS daytime channel A4 vary from 236.0 to 246.9 K, although

most of this difference is due to the later local time of the MCS observations relative to the TES observations. TES observations from MY 24–25 are most similar with an average of 0.3 K brightness temperature difference between channels for both day and night measurements. These 2 years are most similar in terms of instrument and observation characteristics. TES observations from MY 26 and MCS observations from MY 28 are an average of 2.4 and 7.0 K difference for daytime TES MY 26 and MCS MY 28 observations respectively relative to TES MY24. These differences are lower (0.8 and 2.2 K) for nighttime measurements. Much of this difference can be accounted for by the differences in local time (MCS MY 28) and season (TES MY26) of the measurements relative to the TES MY 24–25 observations.

Modeled temperatures closely match the global average MCS and TES temperature measurements (Fig. 6). For measurements equatorward of 60° latitude, the model predicts a cooling of 9.0 (daytime) and 0.9 K (nighttime) for the later local time MCS measurements. After accounting for this modeled cooling, MCS MY 28 temperatures are an average of 0.9 (daytime) and 1.7 K (nighttime) cooler than TES MY 24 measurements (Table 2).

MCS channels A3 (15.4 μm) and A5 (22.2 μm) primarily isolate atmospheric and surface sources of radiance respectively and can be used for comparison between datasets and years. Nighttime measurements between MY 24–28 and TES–MCS vary by 0.7 K and 1.8 K for channels A3 and A5 respectively. This accounts for a predicted cooling of 0.9 K for the MCS A5 surface measurements. Daytime measurements vary by 1.2 K and 3.0 K for channels A3 and A5 respectively, once again accounting for 9 K of cooling for the local time of MCS measurements. Much of this variation is

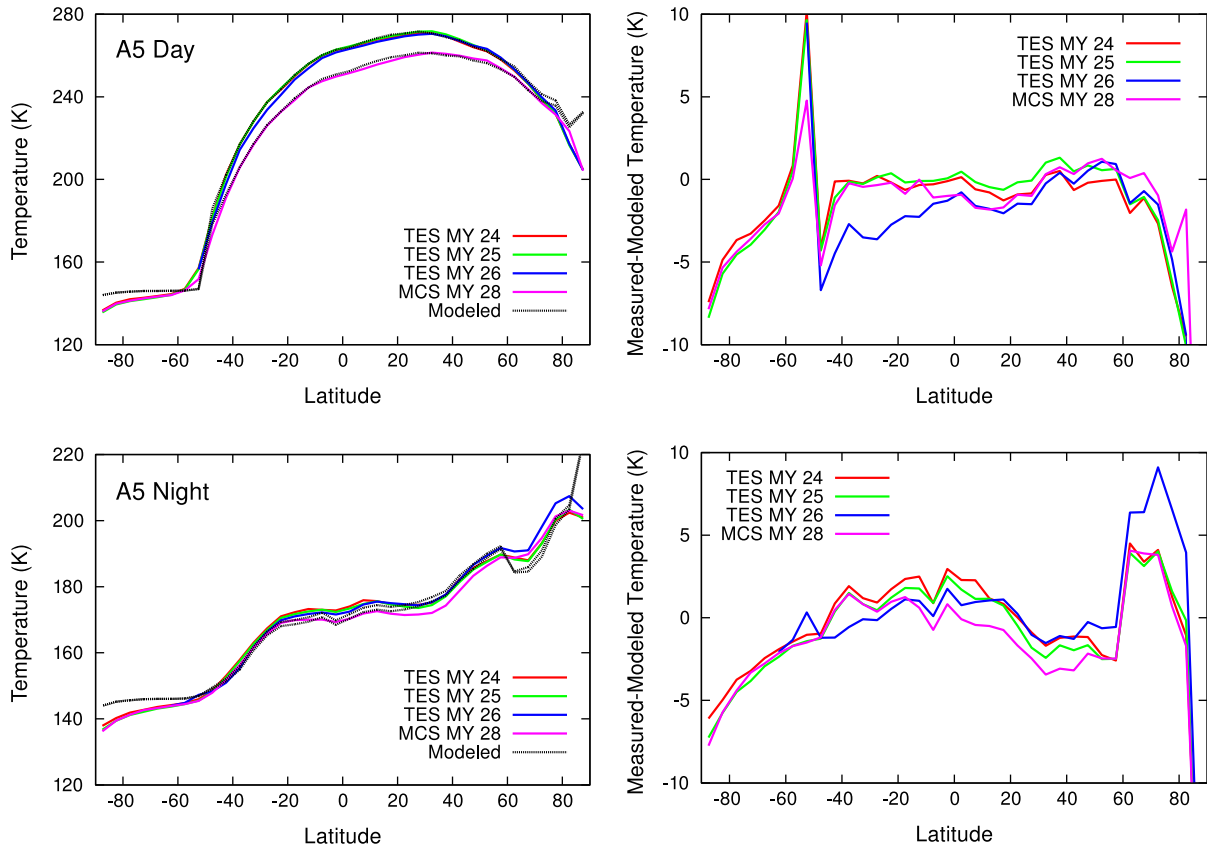


**Fig. 6.** (left) MCS and TES convolved channel A5 longitudinally averaged brightness temperatures with modeled surface temperatures for the 2–3 AM/PM fixed local time of the MCS and MRO orbits, respectively. (right) Measured channel A5 brightness temperatures minus the modeled temperatures shown in the left plots. The deviation between measured and modeled temperatures near 50°S is due to uncertainty in the model of the perennial CO<sub>2</sub> ice cap. Deviations between measured and modeled temperatures near 60–80°N in the nighttime data is due to a slight mismatch in the seasonal time of sunrise between measured and modeled data.

due to TES MY 26 observations that are acquired over a more limited time period than the other TES and MCS measurements.

## 4.2. Visible channel measurements

### 4.2.1. Nadir TES and MCS observations

There are significant regional differences present in the derived albedo between the TES and MCS measurements (Fig. 7). These interannual variations can be greater than 0.05 as has been noted previously within individual datasets (e.g., Smith, 2004; Geissler, 2005). These regional differences are common and comparison of MCS and TES derived Lambert albedos for any given location is likely to show significant differences.

However, despite significant differences within regions, there appears to be little systematic difference on a global level. The global average albedos for MY 24–27 are similar to one another as well as to the MCS derived albedos (Table 3). The global average albedo from MY 24 is slightly lower than the other years and compares most closely to the MCS data with a difference of 0.001 in average albedo. MY 25–27 show albedos about 0.01 higher in

MCS data relative to the TES data. As mentioned above, because of the differences in the MCS and TES solar channel response functions and typical martian reflectance values as a function of wavelength, MCS is expected to have a ~3% higher albedo. The MY 25–27 TES and MY 28 MCS data show a 3.9% difference (~0.23 for TES versus ~0.24 for MCS), which is close to what is expected.

Although MY 24 TES and MY 28 MCS average albedos have the closest values, the MCS data are more consistent with MY 25–27 TES data because of the differences in the instrument response functions (see Section 3). Without accounting for these differences, it might be concluded that Mars may have returned to a global albedo matching MY 24. Rather, it is probable that MY 28 was similar to MY 25–27.

### 4.2.2. Limb aerosol abundance retrievals

A series of three visible channel MCS limb measurements acquired over a period of 178 s at  $L_s$  165 were used to retrieve aerosol abundances as a function of altitude (Figs. 8 and 9). The tangent points for the limb measurements are near 353°E from 3°S to 6°N. Retrieved extinctions are elevated for the lower 20 km of the atmosphere with extinctions  $\geq 0.01 \text{ km}^{-1}$ . There is an additional persistent, but lower opacity ( $0.004\text{--}0.005 \text{ km}^{-1}$ ) layer near 40 km altitude in all of the measurements. A much lower opacity ( $0.0002\text{--}0.0003 \text{ km}^{-1}$ ) layer is present at altitudes of ~65–75 km. The apparent height of this layer is variable, but systematically increases and then decreases over the course of a series of limb measurements. This indicates the presence of an aerosol layer of limited lateral extent as its apparent height variability is due to the curvature of the planet, where the maximum apparent height indicates the actual altitude. This geometric effect is generally negligible for the lower altitude aerosol layers.

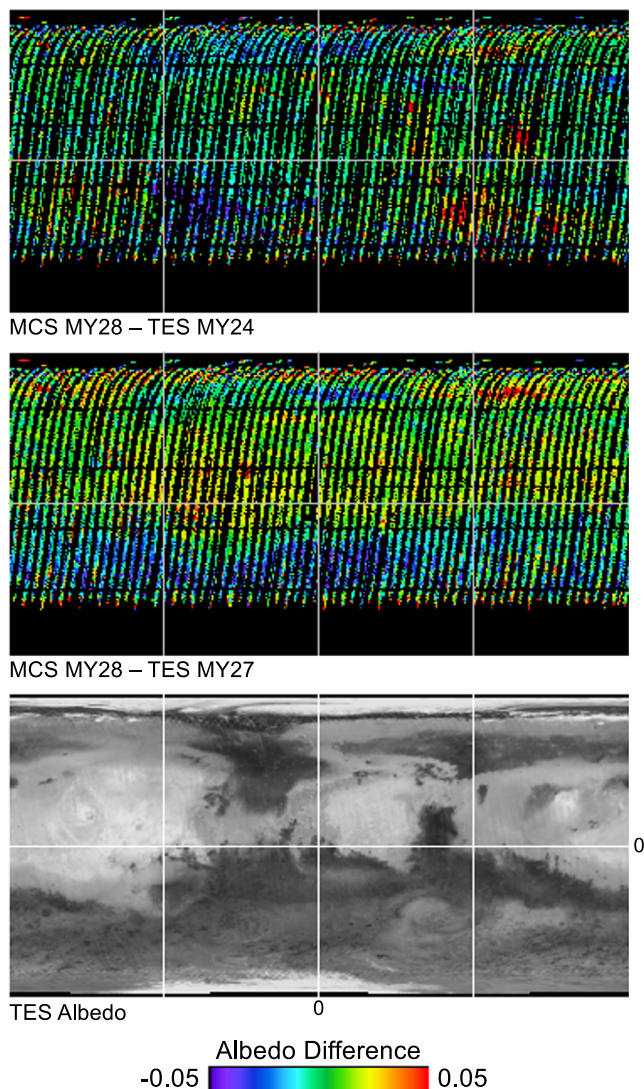


**Fig. 7.** (top) Global Lambert albedo difference maps between TES and MCS visible channel measurements. The TES global albedo map is provided for spatial reference (lower left). Significant differences in regional albedo are present and common from year to year, though globally averaged albedos do not appear to be highly variable.

**Table 3**

Comparison of MCS and TES global average albedo values. MCS and TES data were restricted to latitude/longitude/ $L_s$  bins where both instruments contain a measurement (resulting in slightly different albedo values for MY 28 MCS data for comparison to each TES year).

Martian year	TES albedo	MCS MY 28 albedo	MCS–TES	% Difference
MY 24	0.238	0.238	0.001	0.3
MY 25	0.232	0.241	0.009	3.7
MY 26	0.222	0.231	0.009	3.8
MY 27	0.235	0.246	0.010	4.2

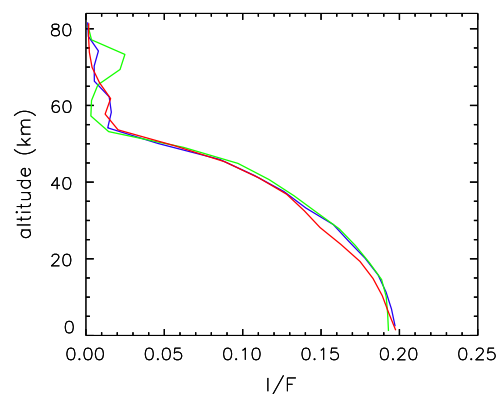


**Fig. 8.** MCS visible channel limb measurements at  $L_s$  165 (MY 28), 353°E, 3°S (red – MRO SCLK 853046355), 0°N (green – SCLK 853046424), and 6°N (blue – SCLK 853046533). (For interpretation of the references to color in this figure legend, the reader is referred to the web version of this article.)

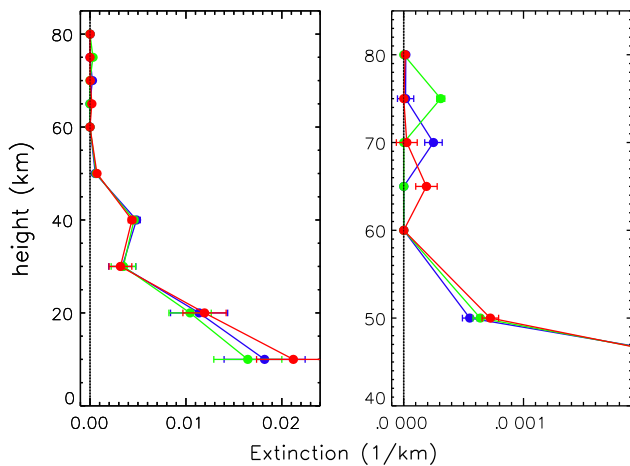


**Fig. 9.** Retrieved aerosol abundances (in extinction, or  $\text{km}^{-1}$ ) for the three MCS limb measurements shown in Fig. 8 (red – SCLK 853046355; green – SCLK 853046424; blue – SCLK 853046533). The left panel shows the full profile that shows the presence of relatively high abundances of dust (<30 km height) and water-ice (near 40 km). The right panel shows detailed abundances retrieved above 40 km where an aerosol layer of limited extent is present above 60 km heights. (For interpretation of the references to color in this figure legend, the reader is referred to the web version of this article.)

## 5. Implications for martian climate monitoring

### 5.1. Interpretation of thermal infrared differences

Although systematic differences of several Kelvin are present between Mars Years in the TES and MCS datasets, these can all be accounted for by systematic differences or calibration uncertainties in the datasets themselves. Both MCS and TES have similar stated absolute accuracies ( $\sim 4 \times 10^{-8} \text{ W cm}^{-2} \text{ sr}^{-1} \text{ cm}^{-1}$  for TES; Christensen et al., 2001; 0.5% for MCS; McCleese et al., 2007). This results in uncertainties of 0.5–1.0 K for daytime measurements and  $\sim 1.0$ –1.5 K for nighttime and atmospheric measurements. Uncertainties are somewhat higher at  $\sim 2.0$ –2.5 K for channel A4 (11.8  $\mu\text{m}$ ) nighttime measurements because of the low radiance at cold temperatures at these relatively short wavelengths. In addition, significantly larger, but poorly understood systematic uncertainties are present in the MY 26 TES dataset.

Given these uncertainties, the differences in seasonal sampling of TES MY 26 observations, and differences in the local time of MCS observations, it is clear that no definitive trend is present in the data. Between the two instrument datasets that cover identical spectral regions and acquire systematic measurements from similar near-polar orbits, differences must be greater than  $\sim 1$ –3 K to be clearly attributed to natural variations in the martian climate.

Smith (2004) investigated global average surface and atmospheric temperatures using TES data from MY 24–26, with a planet encircling dust event occurring during MY 25 ( $L_s \sim 180$ –300). Among the observations made was a  $\sim 3$  K decrease in day and night atmospheric and surface temperatures between MY 25 and MY 26, which was attributed to effects of the global dust event. It is now known that this change coincided with an incorrect calibration procedure (described above) that has since been corrected. As shown in Table 2, there is no systematic difference in brightness temperatures in MY 26 versus MY 25 or 24.

This result is somewhat surprising given the large regional albedo and surface temperature differences that remain valid despite the calibration errors inherent in the data of Smith (2004) that are common across the planet between MY25 and MY 26. It appears that the global redistribution of dust across martian surfaces results in a close to zero net effect on global temperatures, at least

during the time periods investigated here. Spatial, diurnal, and seasonal variations in surface and atmospheric temperatures are common and must be accounted for in order to identify any true global trend.

### 5.2. Interpretation of albedo differences

The TES visible bolometer measurements are more stable than the spectrometer measurements and there are no increased uncertainties in the measurements for MY 26 and 27 relative to MY 24 and 25. Variations in Lambert albedo of 0.015 ( $\sim 6\%$ ) are present between the TES and MCS albedo measurements. This is significantly greater than the uncertainties inherent in the measurements (1–2% in TES; Christensen et al., 2001).

The systematically higher albedos derived from MCS measurements relative to the TES data are consistent with the spectral response of Mars and the slight differences in the shape of the spectral response functions of the TES and MCS measurements. This difference is despite the fact that both instruments have a similar spectral range and shape of their respective response functions.

Previous studies have compared TES and IRTM albedo measurements (Szwast et al., 2006; Fenton et al., 2007; Geissler, 2005). As also shown here, Szwast et al. (2006) noted that global albedo values are highly variable from year to year and they pointed out that comparison of Viking and MGS era albedos using data acquired from limited time periods is complicated by this short term variability. Although certain regions are known to have clearly brightened or darkened, the net global trend in albedo remains unknown over longer periods and has not been disentangled from short term variability. In addition, previous studies have not considered the effects of the spectral response function on the derived albedo values, which are shown here to be significant even for measurements covering similar spectral ranges.

Regional variations in albedo (Fig. 7) are substantial. For example, large portions of the southern hemisphere between  $\sim 10$ – $45^\circ\text{S}$  show a decrease in albedo of up to  $\sim 0.05$  between MY 27 and 28. During the same period, equatorial and northern hemisphere surfaces show a moderate increase (less than  $\sim 0.03$ ) in albedo. These variations in albedo are not restricted to any particular surface type and both bright and dark regions can experience interannual increases or decreases in albedo.

Local areas on Mars have been known to experience substantial albedo changes (e.g., Geissler, 2005). For example, the Cerberus region centered near  $205^\circ\text{E}$ ,  $12^\circ\text{N}$  was a typical dark region imaged by the Viking spacecraft that is largely absent in MGS and MRO images. These dynamic changes over large regions are caused by deposition or scouring of thin (likely just a few microns thick) mantles of dust. The albedo difference maps (Fig. 7) show that these substantial changes in regional albedo continued in the time between the acquisition of the TES and MCS visible bolometer measurements. In particular, the Vastitas Borealis and Utopia Planitia regions within the northern lowlands show distinct changes in albedo that are similar in nature to those recorded between the Viking and MGS eras (Geissler, 2005). It appears that certain regions of Mars are highly susceptible to large and frequent changes in albedo. Collection of long-term, multiannual albedo measurements can be used to reveal the potential frequency and extent of these changes.

The measurements have inherent uncertainties, spatial and temporal sampling biases, and variations in spectral sensitivity. In order to glean any long term trend in global temperature or albedo, it is necessary to acquire continuous and consistent measurements, preferably with overlap between different instruments to cross-calibrate the measurements. Fenton et al. (2007) used a comparison of MGS and Viking era albedos as an in-

put to global circulation model and concluded that the martian climate had warmed between the two eras. However, their study did not take into account potential differences in the spectral response or in the processing of the data (e.g., IRTM-based albedo maps do not assume a Lambert phase function, while TES-based maps do). In addition, only a single year of TES data and 2 years of IRTM data were used in the comparison. The high interannual variability in global albedo acquired during relatively quiet non-dusty periods between MY 24–28 shows that long-term trends cannot be determined from a sampling period of 1–2 years.

### 5.3. Use of off-nadir observations

The vast majority of the MCS dataset is composed of limb and high emission angle observations. These observations are relatively unique because CRISM data is typically acquired from a nadir orientation. Accurate radiance values determined for the MCS solar channel data allow for more detailed studies to determine aerosol properties (similar to the use of TES solar channel data described in Clancy et al. (2003)). The MCS dataset is a systematic and stable multi-annual dataset. Although nadir measurements unfortunately cannot be systematically acquired, the atmospheric monitoring capabilities remain possible with the off-nadir and limb measurements.

Our example limb aerosol abundance retrievals using MCS visible channel measurements illustrate this potential well. Three separate aerosol layers are apparent in the series of observations (Fig. 9). A high opacity layer is concentrated in the lower 30 km of the atmosphere that is likely due to the ubiquitous martian dust. The relatively confined second layer present near 40 km altitude is likely water–ice associated with the last stage of the so-called Aphelion Cloud Belt (e.g., Clancy et al., 1996; Wolff et al., 1999; Pearl et al., 2001).

The third layer appears to be confined with respect to altitude and occurs near the peak altitude observed in the sequence of measurements (~75 km). The occurrence of this layer is similar in both season ( $L_s$  165) and location to equatorial CO<sub>2</sub> ice clouds that have been noted in previous studies (e.g., Clancy et al., 2007; Montmessin et al., 2007; Scholten et al., 2010; Määttänen et al., 2010; Vincendon et al., 2011). These studies used either TES limb measurements, which have limited spatial (typically every 10° of latitude) and vertical sampling (~10 km), or higher spatial resolution, but more sporadically acquired CRISM and OMEGA measurements. The nearly continuous MCS limb observations with 5 km vertical sampling provides a highly complementary dataset that can be used to more fully characterize these aerosols.

It is clearly unrealistic to model limb dust, water ice, and CO<sub>2</sub> aerosols from 0 to 80 km altitude assuming a single composition and particle size distribution and a more sophisticated set of parameters could be included in the retrievals. Nevertheless, given that the results presented here were computed on a time scale of minutes, such an approach could easily be used to map the basic properties (location, height, approximate optical depth) in an efficient and systematic manner.

## 6. Conclusions

MCS nadir oriented thermal infrared and solar channel measurements have been compared with TES measurements across multiple Mars Years. Day and night surface and atmospheric temperatures are within 3 K over the course of 5 martian years after accounting for the local time differences. Any potential interannual variations in temperature are masked by calibration and modeling uncertainties. Smith (2004) attributed interannual global surface and atmospheric temperature variations to major dust storm activ-

ity; however, this variation has since been attributed to a calibration error in the TES dataset that has since been corrected.

The MCS solar channel measurements have been calibrated using CRISM observations to provide a consistent gain factor. Derived Lambert albedos are slightly higher than TES measurements acquired over the same season and locations. Most of this difference can be attributed to differences between the spectral response functions of MCS and TES. Although the measurements cover similar spectral ranges, differences in relative sensitivity at various wavelengths and the spectral dependence of the reflectance of Mars will result in 3% higher MCS albedo values. Consistent with previous work, global albedo is highly variable (~6%) from year to year. This variability must be taken into account when determining long term global trends and the determination of any potential climate trends requires careful analysis of consistent and long term datasets.

Finally, we have demonstrated the potential of the MCS visible channel limb measurements for the characterization of aerosol layers in the martian atmosphere. The MCS dataset represents a systematic set of well-calibrated visible through thermal infrared wavelength measurements of the martian limb. The MCS experiment extends the set of high-quality radiometric measurements of Mars that have been collected nearly continuously from 1998 to the present day.

The MCS and TES measurements are a remarkable series of data that have proven invaluable for studies of the martian climate. However, as on Earth, it is likely that undetected subtle variations in temperature and albedo may be associated with changes in martian weather and climate. In order to capture these variations, long-term and systematic collection of well-calibrated measurements by well-characterized radiometers is necessary. Although the MCS and TES investigations were not designed for long-term climate monitoring, they can serve as an initial study to help define the requirements for future measurements. In particular, especially with respect to MCS, measurement accuracy is not so much the limiting factor as is the need for consistent observations with spatial, temporal, and spectral overlap between spacecraft missions.

## Acknowledgments

We would like to thank the MGS and MRO spacecraft operations teams for ensuring successful science investigations. J.-B. Madeleine and an anonymous reviewer provided helpful and constructive comments that significantly improved this manuscript. This work was partially funded by the MRO Participating Scientist program and JPL Contract 130685 to J.L.B.

## References

- Bandfield, J.L., Edwards, C.S., 2008. Derivation of martian surface slope characteristics from directional thermal infrared radiometry. *Icarus* 193, 139–157. <http://dx.doi.org/10.1016/j.icarus.2007.08.028>.
- Bandfield, J.L., Feldman, W.C., 2008. Martian high latitude permafrost depth and surface cover thermal inertia distributions. *J. Geophys. Res.* 113, E08001. <http://dx.doi.org/10.1029/2007JE003007>.
- Bell, J.F. et al., 2009. Mars Reconnaissance Orbiter Mars Color Imager (MARCI): Instrument description, calibration, and performance. *J. Geophys. Res.* 114, E08S92. <http://dx.doi.org/10.1029/2008JE003315>.
- Cantor, B. et al., 2002. Multiyear Mars Orbiter Camera (MOC) observations of repeated martian weather phenomena during the northern summer season. *J. Geophys. Res.* 107, 5014. <http://dx.doi.org/10.1029/2001JE001588>.
- Christensen, P.R. et al., 1992. Thermal emission spectrometer experiment – Mars Observer mission. *J. Geophys. Res.* 97, 7719–7734. <http://dx.doi.org/10.1029/92JE00453>.
- Christensen, P.R. et al., 2001. Mars Global Surveyor Thermal Emission Spectrometer experiment: Investigation description and surface science results. *J. Geophys. Res.* 106, 23823–23872. <http://dx.doi.org/10.1029/2000JE001370>.
- Clancy, R.T. et al., 1996. Water vapor saturation at low altitudes around Mars aphelion: A key to Mars climate? *Icarus* 122, 36–62. <http://dx.doi.org/10.1006/icar.1996.0108>.

- Clancy, R.T. et al., 2000. An intercomparison of ground-based millimeter, MGS TES, and Viking atmospheric temperature measurements: Seasonal and interannual variability of temperatures and dust loading in the global Mars atmosphere. *J. Geophys. Res.* 105, 9553–9572. <http://dx.doi.org/10.1029/1999JE001089>.
- Clancy, R.T. et al., 2003. Mars aerosol studies with the MGS TES emission phase function observations: Optical depths, particle sizes, and ice cloud types versus latitude and solar longitude. *J. Geophys. Res.* 108, 5098. <http://dx.doi.org/10.1029/2003JE002058>.
- Clancy, R.T. et al., 2007. Mars equatorial mesospheric clouds: Global occurrence and physical properties from Mars Global Surveyor Thermal Emission Spectrometer and Mars Orbiter Camera limb observations. *J. Geophys. Res.* 112, E04004. <http://dx.doi.org/10.1029/2006JE002805>.
- Curran, R.J., Conrath, B.J., Hanel, R.A., Kunde, V.G., Pearl, J.C., 1973. Mars: Mariner 9, spectroscopic evidence for H<sub>2</sub>O ice clouds. *Science* 182, 381–383. <http://dx.doi.org/10.1126/science.182.4110.381>.
- Fenton, L.K. et al., 2007. Global warming and climate forcing by recent albedo changes on Mars. *Nature* 446, 646–649. <http://dx.doi.org/10.1038/nature05718>.
- Ferguson, R.L. et al., 2006. High-resolution thermal inertia derived from the Thermal Emission Imaging System (THEMIS): Thermal model and applications. *J. Geophys. Res.* 111, E12004. <http://dx.doi.org/10.1029/2006JE002735>.
- Geissler, P.E., 2005. Three decades of martian surface changes. *J. Geophys. Res.* 110, E02001. <http://dx.doi.org/10.1029/2004JE002345>.
- Glenar, D.A., Samuelson, R.E., Pearl, J.C., Bjoraker, G.L., Blaney, D., 2003. Spectral imaging of martian water ice clouds and their diurnal behavior during the 1999 aphelion season ( $L_s = 130 \pm 125$ ). *Icarus* 161, 297–318. [http://dx.doi.org/10.1016/S0019-1035\(02\)00046-5](http://dx.doi.org/10.1016/S0019-1035(02)00046-5).
- Herman, B.M. et al., 1994. Numerical technique for solving the radiative transfer equation for a spherical shell atmosphere. *Appl. Opt.* 33 (9), 1760–1770. <http://dx.doi.org/10.1364/AO.33.001760>.
- Herman, B.M., Flittner, D.E., Caudill, T.R., Thome, K.J., Ben-David, A., 1995. Comparison of the Gauss-Seidel spherical polarized radiative transfer code with other radiative transfer codes. *Appl. Opt.* 34 (21), 4563–4572. <http://dx.doi.org/10.1364/AO.34.004563>.
- Hinson, D.P. et al., 1999. Initial results from radio occultation measurements with Mars Global Surveyor. *J. Geophys. Res.* 104, 26997–27012. <http://dx.doi.org/10.1029/1999JE001069>.
- Jakosky, B.M., Farmer, C.B., 1982. The seasonal and global behavior of water vapor in the Mars atmosphere – Complete global results of the Viking atmospheric water detector experiment. *J. Geophys. Res.* 87, 2999–3019. <http://dx.doi.org/10.1029/JB087iB04p02999>.
- Kieffer, H.H., 2013. Thermal model for analysis of Mars infrared mapping. *J. Geophys. Res.* <http://dx.doi.org/10.1029/2012JE004164>.
- Liu, J. et al., 2003. An assessment of the global, seasonal, and interannual spacecraft record of martian climate in the thermal infrared. *J. Geophys. Res.* 108, 5089. <http://dx.doi.org/10.1029/2002JE001921>.
- Loughman, R.P. et al., 2004. Comparison of radiative transfer models for limb-viewing scattered sunlight measurements. *J. Geophys. Res.* 109, D06303. <http://dx.doi.org/10.1029/2003JD003854>.
- Määttänen, A. et al., 2010. Mapping the mesospheric CO<sub>2</sub> clouds on Mars: MEX/OMEGA and MEX/HRSC observations and challenges for atmospheric models. *Icarus* 209, 452–469. <http://dx.doi.org/10.1016/j.icarus.2010.05.017>.
- Madeleine, J.-B. et al., 2012. Aphelion water–ice cloudmapping and property retrieval using the OMEGA imaging spectrometer onboard Mars Express. *J. Geophys. Res.* 117. <http://dx.doi.org/10.1029/2011JE003940>.
- Markwardt, C.B., 2009. “Non-linear Least-squares Fitting in IDL with MPPFIT” *Astronomical Data Analysis Software and Systems XVIII ASP Conference Series*, vol. 411. In: Bohlender, David A., Durand, Daniel, Dowler, Patrick (Eds.), *Proceedings of the Conference held 2–5 November 2008 at Hotel Loews Le Concorde, Quebec City, QC, Canada*. Astronomical Society of the Pacific, San Francisco, 2009, p. 251.
- Martin, T.Z., 1981. Mean thermal and albedo behavior of the Mars surface and atmosphere over a martian year. *Icarus* 45, 427–446. [http://dx.doi.org/10.1016/0019-1035\(81\)90045-2](http://dx.doi.org/10.1016/0019-1035(81)90045-2).
- Martin, T.Z., Richardson, M.I., 1993. New dust opacity mapping from Viking Infrared Thermal Mapper data. *J. Geophys. Res.* 98, 10. <http://dx.doi.org/10.1029/93JE01044>.
- McCleese, D.J. et al., 2007. Mars climate sounder: An investigation of thermal and water vapor structure, dust and condensate distributions in the atmosphere, and energy balance of the polar regions. *J. Geophys. Res.* 112, E05S06. <http://dx.doi.org/10.1029/2006JE002790>.
- Montmessin, F. et al., 2007. Hyperspectral imaging of convective CO<sub>2</sub> ice clouds in the equatorial mesosphere of Mars. *J. Geophys. Res.* 112, E11S90. <http://dx.doi.org/10.1029/2007JE002944>.
- Moré, J., 1978. The Levenberg–Marquardt Algorithm: Implementation and theory. In: Watson, G.A. (Ed.), *Numerical Analysis*. Springer-Verlag, Berlin, pp. 105–116. <http://dx.doi.org/10.1007/BFb0067700>.
- Murchie, S. et al., 2007. Compact Reconnaissance Imaging Spectrometer for Mars (CRISM) on Mars Reconnaissance Orbiter (MRO). *J. Geophys. Res.* 112, E05S03. <http://dx.doi.org/10.1029/2006JE002682>.
- Pearl, J.C. et al., 2001. Observations of martian ice clouds by the Mars Global Surveyor Thermal Emission Spectrometer: The first martian year. *J. Geophys. Res.* 106, 12325–12338. <http://dx.doi.org/10.1029/1999JE001233>.
- Petrova, E., Keller, H.U., Markiewicz, W.J., Thomas, N., Wuttke, M.W., 1996. Ice hazes and clouds in the martian atmosphere as derived from the Phobos/KRFM data. *Planet. Space Sci.* 44, 1163–1176. [http://dx.doi.org/10.1016/S0032-0633\(96\)00029-3](http://dx.doi.org/10.1016/S0032-0633(96)00029-3).
- Richardson, M.I., 1998. Comparison of microwave and infrared measurements of martian atmospheric temperatures – Implications for short-term climate variability. *J. Geophys. Res.* 103, 5911. <http://dx.doi.org/10.1029/97JE03372>.
- Scholten, F. et al., 2010. Concatenation of HRSC colour and OMEGA data for the determination and 3D-parameterization of high-altitude CO<sub>2</sub> clouds in the martian atmosphere. *Planet. Space Sci.* 58 (10), 1207–1214. <http://dx.doi.org/10.1016/j.pss.2010.04.015>.
- Smith, M.D., 2002. The annual cycle of water vapor on Mars as observed by the thermal emission spectrometer. *J. Geophys. Res.* 107, 5115. <http://dx.doi.org/10.1029/2001JE001522>.
- Smith, M.D., 2004. Interannual variability in TES atmospheric observations of Mars during 1999–2003. *Icarus* 167, 148–165. <http://dx.doi.org/10.1016/j.icarus.2003.09.010>.
- Szwast, M.A. et al., 2006. Surface dust redistribution on Mars as observed by the Mars Global Surveyor and Viking orbiters. *J. Geophys. Res.* 111, E11008. <http://dx.doi.org/10.1029/2005JE002485>.
- Tamppari, L.K., Zurek, R.W., Paige, D.A., 2003. Viking-era diurnal water–ice clouds. *J. Geophys. Res.* 108, 5073. <http://dx.doi.org/10.1029/2002JE001911>.
- Titus, T.N. et al., 2003. Exposed water ice discovered near the south pole of Mars. *Science* 299, 1048–1051. <http://dx.doi.org/10.1126/science.1080497>.
- Vincendon, M. et al., 2011. New near-IR observations of mesospheric CO<sub>2</sub> and H<sub>2</sub>O clouds on Mars. *J. Geophys. Res.* 116, E00J02. <http://dx.doi.org/10.1029/2011JE003827>.
- Wilson, R.J., Richardson, M.I., 2000. The martian atmosphere during the Viking mission. I. Infrared measurements of atmospheric temperatures revisited. *Icarus* 145, 555. <http://dx.doi.org/10.1006/icar.2000.6378>.
- Wilson, R.J., Neumann, G.A., Smith, M.D., 2007. Diurnal variation and radiative influence of Martian water ice clouds. *Geophys. Res. Lett.* 34. <http://dx.doi.org/10.1029/2006GL027976>.
- Withers, P., Smith, M.D., 2006. Atmospheric entry profiles from the Mars Exploration Rovers Spirit and Opportunity. *Icarus* 185, 133–142. <http://dx.doi.org/10.1016/j.icarus.2006.06.013>.
- Wolff, M.J. et al., 1999. Hubble Space Telescope observations of the martian aphelion cloud belt prior to the Pathfinder mission: Seasonal and interannual variations. *J. Geophys. Res.* 104, 9027–9042. <http://dx.doi.org/10.1029/98JE019>.
- Wolff, M.J. et al., 2006. Constraints on dust aerosols from the Mars Exploration Rovers using MGS overflights and Mini-TES. *J. Geophys. Res.* 111, E12S17. <http://dx.doi.org/10.1029/2006JE002786>.
- Wolff, M.J. et al., 2009. Wavelength dependence of dust aerosol single scattering albedo as observed by the Compact Reconnaissance Imaging Spectrometer. *J. Geophys. Res.* 114, E00D04. <http://dx.doi.org/10.1029/2009JE003350>.
- Zasova, L., Grassi, D., Formisano, V., Maturilli, A., 2001. The martian atmosphere in the region of the great volcanoes: Mariner 9 IRIS data revisited. *Planet. Space Sci.* 49, 977–992. [http://dx.doi.org/10.1016/S0032-0633\(01\)00040-X](http://dx.doi.org/10.1016/S0032-0633(01)00040-X).